

Pt/Ni single-atom alloy boosts mechano-pyrolysis of alkane into hydrogen

Rui Tu¹, Jikai Sun¹, Yuchun Xu, Hongyan Yang, Xu Fang, Ling Zhang, Junxia Yang, Guoqing Ren, Xiuqin Ci, Weiqiao Deng, Tie Yu*

Institute of Molecular Sciences and Engineering, Institute of Frontier and Interdisciplinary Science, Shandong University, Qingdao, Shandong 266237, China



ARTICLE INFO

Keywords:
Hydrogen Production
Methane Pyrolysis
Mechanochemistry
Single-Atom Alloy
Carbon product

ABSTRACT

Mechanochemistry approach was utilized to solve the carbon deposition during alkane pyrolysis process. Pt/Ni single-atom alloy (SAA) was constructed on Ni balls surface as catalyst and grinding medium simultaneously, and physical collision of metallic balls generated mechanical energy to remove the deposited carbon and accelerate reaction rates. XANES spectra proved Pt/Ni SAA structure on the Ni ball surface, and its turnover frequency (TOF) was 1530 h^{-1} under 1 atm and 450 °C without by-products. An extremely long lifetime of methane pyrolysis at least 350 h on stream has been obtained. This Pt/Ni SAA was also active for mechano-pyrolysis of ethane/propane, and DFT calculations confirmed that the improvement of catalytic efficiency originated from the d-band center up-shifting under mechanic stress on Pt/Ni SAA surface. This mechanical catalysis study provides an alternative route for clean hydrogen production and a strategy for deposited carbon removal under mechanical conditions.

1. Introduction

Mechanochemistry is an emerging chemical technology that supplies a new driving force to induce and catalyze a range of chemical reactions [1–4]. Specifically, the movement of metallic balls in ball grinder induces medium deformation and subsequently generates mechanical energy, which activates and converts the reactants into products in a circulating up-and-down motion, if the presence of catalyst is involved in this process, it is also known as mechanical catalysis [5]. Compared to other conventional catalysis methods, mechanical catalysis exhibits distinctive characteristics. The impact force generated by mechanical motion could cause the formation of high-defect sites on the grinding medium [6,7], thereby enabling reactions that are typically challenging to occur at low temperatures. These defect sites provide more exposed active centers, which could effectively adsorb and activate reactant molecules [8]. Meanwhile, the defect sites effectively reduce the activation energy of chemical reaction through adjusting the electronic structure and adsorption capacity during physical grinding process [9]. Recently, mechanical catalysis method has been successfully applied to synthesize ammonia from N₂ and H₂, and the reports noted mechanical energy could activate N₂ more efficiently. Specifically, the efficiency of ammonia yield would increase as the mechanical energy strengthens via the control of vibration frequency, indicating this method greatly

moderates the reaction conditions in batch reaction system [10]. In addition, the mechanical catalysis method involves collision and shearing between grinding balls, which may potentially exert additional effects to solve carbon deposition on active sites and other catalyst deactivation issues during specific reactions.

Alkane pyrolysis is one of the methods to produce hydrogen without carbon emission. Previous literature revealed that direct thermal pyrolysis of methane was implemented around 1300 °C to achieve a satisfactory H₂ yield [11]. The application of metal-based catalysts during pyrolysis reaction could decrease the methane pyrolysis temperature fairly. In particular, Fe- [12], Co- [13] or Ni- [14] based catalysts exhibited good catalytic activity still need to be above 600 °C. Nevertheless, the high operating temperature would induce the metal sintering under reducing atmosphere and the generated carbon powder could cover the active sites, which both lead to catalysts deactivation with time on stream. Besides, the high energy consumption of the pyrolysis reaction also impedes its scalability [15]. Therefore, the current challenge for this pyrolysis approach lies in effectively inhibiting the catalyst deactivation and reducing the temperature of alkane pyrolysis reactions while simultaneously achieving optimal yields. In order to address the aforementioned issues, we proposed a mechano-pyrolysis approach to achieve alkanes cracking under milder reaction conditions and enhance catalyst stability. During the initial phase, we

* Corresponding author.

E-mail address: yutie@sdu.edu.cn (T. Yu).

¹ These authors equally contributed to this work

extensively investigated various forms of catalysts and ultimately opted for single-atom alloy (SAA) as an ideal choice for coupling with mechanical catalysis.

Single-atom catalyst (SAC) have garnered significant attention due to their exceptional atomic utilization, activity and selectivity [16–18]. The formation of SAA, achieved by dispersing isolated metal atoms onto the surface of other metallic substrates, combines the advantageous features of both SAC and alloy with robust structure stability [19]. The application of SAA has been extensively investigated in the fields of hydrogenation [20], dehydrogenation [21], oxidation [22], and hydrogenolysis [23]. It has been documented that single atomically dispersed metal catalyst presented excellent catalytic performance compared to the nanosized metal catalyst for more exposed sites and so on [24,25]. Considering aforementioned issues for alkane pyrolysis reaction, we assume that active sites could be anchored on metallic ball surface to form SAA as grinding medium and catalyst simultaneously and improve their stability, meanwhile, mechanical energy can be introduced into the alkane cracking reaction to enhance catalytic efficiency and lower the temperature required for pyrolysis.

In this work, Pt/Ni SAA was synthesized by loaded Pt atoms on nickel metallic balls. Then, the Pt/Ni SAA was packaged in a homemade ball milling reactor for methane mechano-pyrolysis, compared to pure Ni metallic balls, the addition of Pt exhibits superior catalytic activity (shown in Fig. S1). Its thermal pyrolysis activities of methane under different reaction conditions including temperature and vibration frequency were estimated. A series of complementary bulk characterization techniques including XRD, AFM, EXAFS and XPS studies were utilized to study the SAA structure of Pt/Ni. Subsequently, further DFT calculations were employed to elucidate the mechanism of methane pyrolysis over the Pt/Ni SAA and the contribution of mechanical action to the catalytic reaction. Besides, carbon deposition and catalytic stability over Pt/Ni SAA during the reaction process were conducted through experimental test, and utilization of generated carbon byproducts was explored as catalyst carrier for battery electrode material to improve the atomic-economy of this mechanical catalysis technology. Finally, the reactants were extended to ethane and propane to study their conversion over Pt/Ni SAA, and the advantages of this mechanical catalysis paradigm to produce pure H₂ without coking issue was proposed.

2. Experimental

2.1. Preparation of the Pt/Ni single-atom alloy (SAA) and pure Ni/Ni catalysts

Pure Ni balls were purchased from Hong-Ju metal material Co., Ltd (Hebei, China) and exhibited a weight of 333 g and a diameter of 6–12 mm. Prior to metal loading, the Ni balls were sonicated in DMF for 30 min and washed with deionized water. After drying the Ni balls, they were immersed in a chloroplatinic acid solution (0.0127 M) for 10 h, followed by filtration, drying in air for 30 min, calcination at 850 °C and reduction at 700 °C for 2 h under 20 mL of 10 % H₂/Ar. Pure Ni/Ni catalyst was prepared by the same process, except that Ni(HCOO)₂ solution was used in the impregnation process.

2.2. Sample characterization

Surface areas were determined on a Micromeritics ASAP 2460 using N₂ adsorption isotherms and the BET method. Prior to the measurement, the sample was degassed under vacuum at 200 °C for 8 h. X-ray diffraction (XRD) patterns were recorded on a PANalytical Model Xpert3 instrument equipped with a Cu K α radiation source ($\lambda = 0.15406$ nm) operating at 40 kV and 10 mA. X-ray photoelectron spectroscopy (XPS) was performed using a Thermo Fisher ESCALAB 250Xi spectrometer with a monochromatized Al K α X-ray source (1486.6 eV) and an applied power of 150 W. The C 1 s (binding energy 284.8 eV) was used as a

reference. Pt loading was estimated by inductively coupled plasma-optical emission spectrometry (Agilent 725 ICP-OES). XANES spectra were obtained at the BL14W1 beam line (Beijing Synchrotron Radiation Facility) in transmission mode to obtain Pt L-edge XAS spectra. Pt foil and PtO₂ were collected for comparison and monochromatic energy calibration. Athena software was used to analyze the spectra, and the extracted EXAFS data were weighted by k³ and then converted to R space by FT to obtain magnitude plots for the EXAFS spectra. SEM investigations were performed with a Quanta 250 FEG instrument to study the morphology of the carbon products. Raman spectra of carbon products were acquired with a Thermo Fisher D XR2 spectrometer with an excitation wavelength of 532 nm and a laser power of 8 mW. Prior to the measurements, the Raman spectrometer was calibrated with the silicon peak (520.7 cm⁻¹). A thermal infrared imager (AVIO NEC R450) was utilized to estimate the temperatures of the Ni balls before and after collision, and atomic force microscopy (AFM, SPI 3800 N SPA400) was applied to measure the metal surface morphology.

2.3. Activity test

CH₄ pyrolysis was studied with a homemade mechanical system with an electromotor used to control the vibration frequency of the reactor; the system could support mechanical catalysis below 450 °C and vibration frequencies from 0 to 1500 r/min (motor speed, corresponding to the vibration frequency of the ball milling reactor, was about 0–25 Hz). Typically, 333 g Ni balls were sealed in the reactor, and the temperature was controlled with a type K thermocouple inserted inside the reactor. The feed gas was pure CH₄ with a flow rate of 100 mL/min. The reaction was performed at atmospheric pressure. Prior to activity tests, catalysts were pretreated under 20 % H₂/Ar at 150 °C for 2 h, and then the reactants were introduced into the reactor. For ethane and propane pyrolysis, the inlets compositions were 10 % C₂H₆/90 % N₂ and 10 % C₃H₈/90 % N₂. Detailed procedures for each activity test were shown in the figure caption. The products were analyzed by online GC (ThermoFisher Trace1300), which involved a thermal conductivity detector (TCD) and a flame ionization detector (FID). Porapak Q and 5 Å molecular sieve columns were connected to the TCD, while TG WAXMS and HP AL/S capillary columns were connected to the FID. Oxygenates and hydrocarbons were analyzed by FID, while C₂H₄, Ar, CO and CH₄ were analyzed by TCD. CH₄ was taken as a reference to bridge between FID and TCD. The first sample test was recorded after 10 min of run time. CH₄ conversion and CO_x selectivity were calculated as follows:

$$\text{CH}_4 \text{ conversion} = (\text{CH}_4 \text{ inlet} - \text{CH}_4 \text{ outlet}) / (\text{CH}_4 \text{ inlet}) \times 100\%,$$

where CH₄ inlet and CH₄ outlet represent moles of CH₄ at the inlets and outlets, respectively. For ethane and propane conversion, only CH₄ in equation was replaced by ethane or propane concentrations.

$$\text{CO}_2 \text{ Selectivity} = (2 \times \text{CO}_2 \text{ outlet}) / (\text{H}_2 \text{ outlet}) \times 100\%$$

$$\text{CO Selectivity} = (2 \times \text{CO outlet}) / (\text{H}_2 \text{ outlet}) \times 100\%$$

where CO_x inlet and CO_x outlet represent moles of CO_x at the inlets and outlets. The selectivity of CO and CO₂ was calculated based on the side reactions during the induction period of pyrolysis reaction (CH₄ + 2 [O] = CO₂ + 2 H₂ or CH₄ + [O] = CO + 2 H₂).

The turnover frequency (TOF) of Methane to Hydrogen were calculated as follows:

$$\text{TOF}_{\text{H}_2} = n_{\text{H}_2} / (n_{\text{Pt}} \times t)$$

where n_{H₂} represents the molar of generated hydrogen, n_{Pt} is the total number of Pt metal atoms, and t is the reaction time in hours. For Pt/Ni sample, we have deducted the contribution of Ni ball itself to ensure the accuracy of calculated results, which meant that the calculated CH₄ conversion rate was only attributed to the active Pt species.

2.4. Electrochemical tests

Electrochemical tests of as-synthesized samples and commercial graphite were conducted using CR2032 coin cells with a glass fiber (GF/A, Whatman) and sodium metal sheets as counter electrodes. To obtain working electrodes, a slurry containing the active materials conductive, carbon black and polyvinylidene fluoride (PVDF) with a mass ratio of 7:2:1 in N-methylpyrrolidone (NMP) was coated on steel sheets and dried at 120 °C for 12 h. The electrolyte was 1 M NaPF₆ in ethylene carbonate/dimethyl carbonate/ethyl methyl carbonate (EC: DMC: EMC =1:1:1 in volume). Then, the cells were assembled in an argon-filled glove box with 70 μL of electrolyte. The mass loading of the active material was approximately 1 mg·cm⁻². Galvanostatic charging/discharging tests and cycling stability tests were carried out in a LAND CT3001A battery testing system with a voltage range of 0.01–3 V vs. Na/Na⁺ at room temperature.

3. Results and discussion

3.1. CH₄ mechano-pyrolysis activity

In Fig. 1a, a CH₄ conversion comparison over the Pt/Ni SAA (0.004 g Pt /333 g Ni balls) showed that this catalytic reaction with vibration (500 r/min) exhibited obviously enhanced CH₄ pyrolysis ability at 450 °C compared with that under the static condition. Under vibration condition, the initial efficiency for CH₄ conversion was 6.1 % and was maintained at 5.8 % with the time on stream. While the initial CH₄ conversion under static condition was 3.1 %, and the Pt/Ni SAA was

almost deactivated after 13 h, illustrating that mechanical vibration greatly boosted catalytic activity and elongated its stability simultaneously. The power consumption under mechanical condition and static condition was estimated in Table S1, and it was seen that vibration motor only contributed ~ 1 % energy consumption compared with that under static condition at 450 °C. Nevertheless, the greatly improved CH₄ conversion and coking resistance behavior induced by mechanical energy in Fig. 1a illustrated an intriguing energy efficiency during methane pyrolysis. Fig. 1b lists the CH₄ conversion efficiencies seen with vibration and at temperatures ranging from 360 °C to 450 °C, and the TOF of H₂ in effluent rose with increment of temperature for its exothermic reaction property. Moreover, increasing vibration frequency also accelerated H₂ production, as shown in Fig. 1c. The positive impact of the mechanical action on catalytic CH₄ pyrolysis could be proven by the smaller apparent activation energy (E_a) seen for vibration mode lower than that for static mode (Fig. S2).

3.2. Bulk characterization of Pt/Ni single-atom alloy

Since Pt atoms were designed to anchor on the external surface of Ni ball as shown in Fig. 2a, SEM and EDS images (Fig. 2b, S3 and S4) were taken to observe the morphology and Pt distribution on the Ni metal surface, and the comparison between pristine Ni and Pt/Ni surfaces showed that Pt loading procedure roughened the Ni surface. This variation in roughness was also indicated by the height differences in the AFM images (Fig. 2d and e). The Pt/Ni SAA surface exhibited 890 nm height difference, which was higher than that of the pristine Ni sample (150 nm difference). The XRD profiles in Fig. 2c showed that only peaks

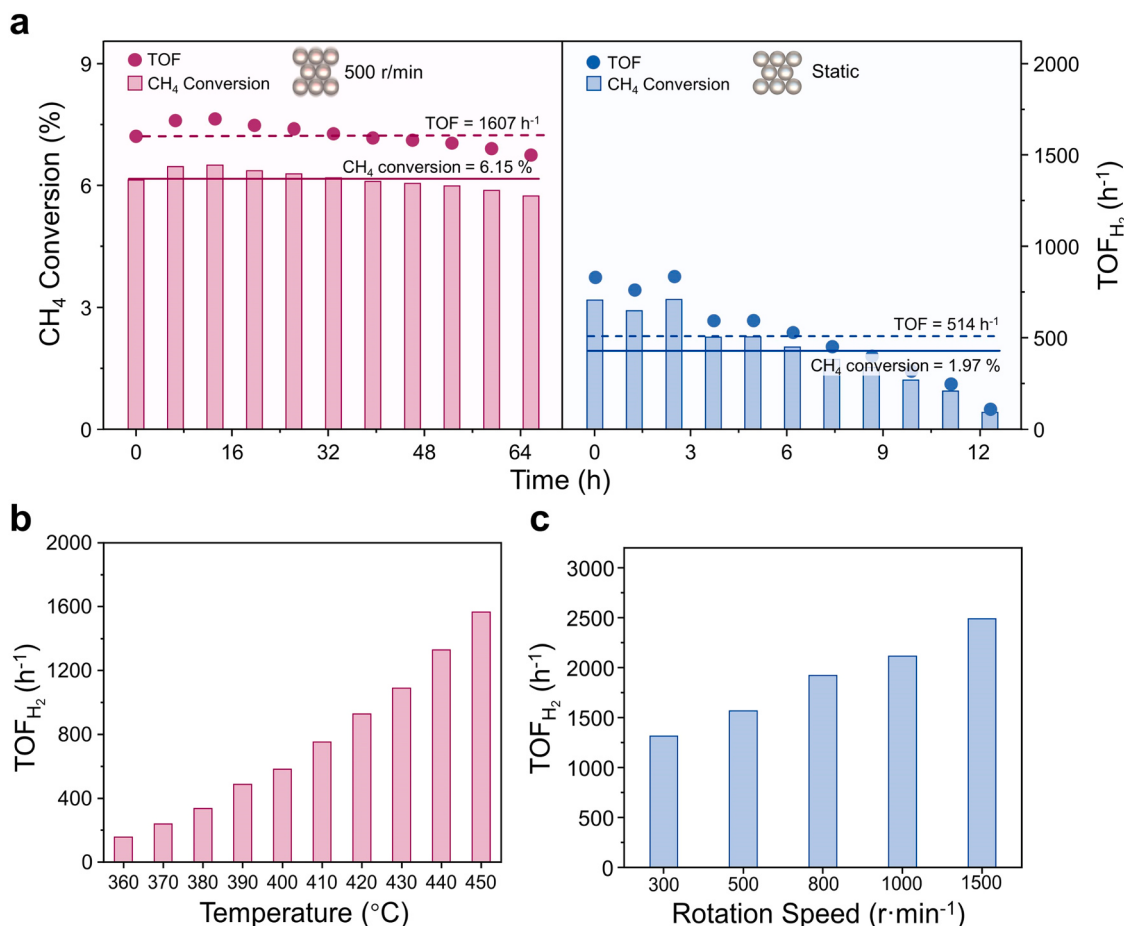


Fig. 1. (a) Comparison CH₄ conversion and TOF in form of H₂ production with or without vibration. Reaction conditions: 100 mL/min CH₄, 450 °C. Under mechanical catalysis condition, the motor vibration frequency was 500 r/min. Under static catalysis condition, the motor vibration frequency was 0 r/min. (b) TOF of H₂ production as a function of reaction temperature from 360 °C to 450 °C. (c) Impact of vibration frequency from 300 r/min to 1500 r/min on the TOF of H₂.

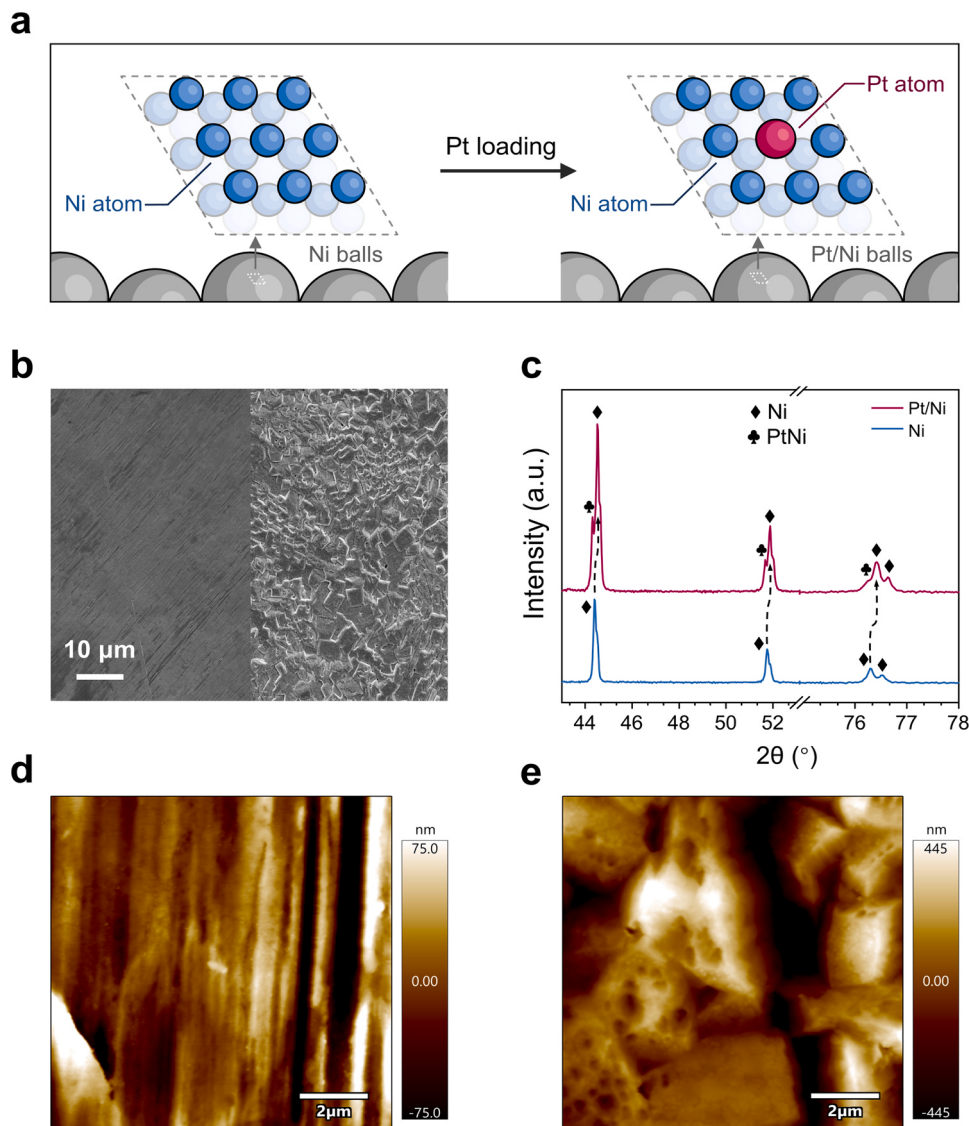


Fig. 2. (a) Schematic diagram of Pt/Ni SAA catalyst preparation. (b) The SEM images of fresh Ni (left) and Pt/Ni SAA (right). (c) XRD profiles of pristine Ni and Pt/Ni SAA. AFM images for (d) the pristine Ni sample and e) the Pt/Ni SAA.

for the Ni fcc structure were detected for pristine Ni balls. These Ni XRD peaks shifted to higher angles after Pt doping, and new peaks, which were assigned to the Pt/Ni alloy, appeared over the Pt/Ni SAA [26–28]. The peak shifts were probably induced by invasion of Pt atoms into Ni crystals.

The XANES data for the Pt L₃-edge in Fig. 3a supplied additional evidence for the Pt/Ni alloy structure. The Pt L₃-edge spectra for Pt/Ni, Pt foil and PtO₂ presented different white line intensities and d-band vacancies. The higher intensity represented a higher chemical valence, and it was confirmed that the Pt atoms were in a reduced state over the Pt/Ni SAA. The slightly lower white line intensity for the Pt/Ni SAA than that for Pt foil was primarily attributed to electron donation from Ni to Pt since Ni atoms possess less electronegative than Pt atoms. Fig. 3b and S5 showed a comparison of EXAFS spectra in k-space and Fourier transform spectra in R-space for Pt/Ni and Pt foil. The R-space spectrum unveiled that the bond length for the first shell on the Pt/Ni SAA was 2.3 Å. The actual bond length was 2.55 Å from the fit profile (Fig. S5d and Table S2), and the coordination number was approximately 6 for the Pt-Ni band. Since this Pt-Ni bond was shorter than the Pt-Pt bond (Fig. 3b and Table S2), generation of the Pt-Ni bond was confirmed here. Pt particles were not observed over Pt/Ni SAA and the various

amplitudes between Pt foil and Pt/Ni SAA in k-space proved no Pt-Pt bond over Pt/Ni SAA (Fig. S5a). Pt 4 f (Fig. 3c) and Ni 2p (Fig. 3d) XPS spectra indicated the valence states of Pt and Ni on the Pt/Ni SAA. Pt was only present as Pt⁰ atoms, while approximately 26 % NiO was recorded in addition to Ni⁰ atoms. Moreover, the observation of an O 1 s XPS signal (Fig. S6) also implied the presence of NiO phase on the milling balls surface, but there was no evidence for PtO₂.

3.3. Reaction mechanism of CH₄ pyrolysis under mechanical conditions

DFT calculations were applied to examine the successive scissions of C-H bonds that convert methane to atomic carbon. Primarily, it was essential to find the optimal configurations for all CH_x species (x = 0, 1, 2, 3, and 4) on Pt/Ni (111) surfaces. As shown in Fig. S7, three adsorption sites were considered for these CH_x adsorbates, namely, atop, bridge, and hollow. The most stable configurations on Pt/Ni (111) SAA are shown in Fig. S8a. In addition, transition states were searched for the C-H bond scission steps converting *CH₄ to *C on Pt/Ni SAA. DFT structures for the C-H bond scission transition states on the Pt/Ni (111) SAA were shown in Fig. S8b. The corresponding energy barriers were provided in Fig. S8c. Specifically, the dehydrogenation step of *CH to *C

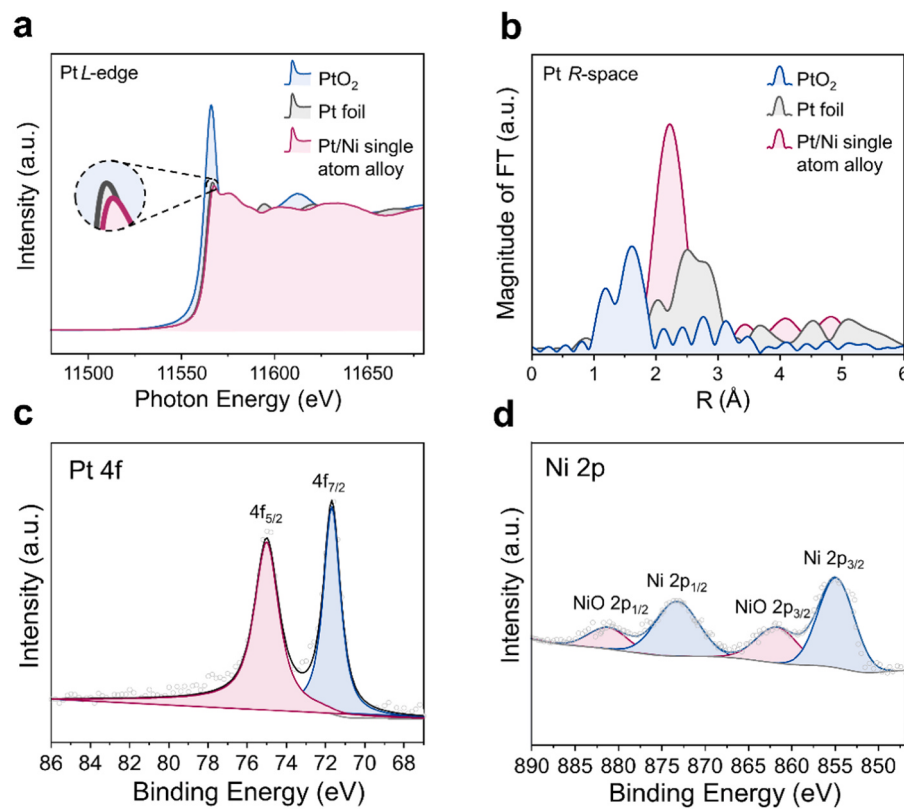


Fig. 3. (a) XANES Pt L₃-edge data for Pt foil, Pt/Ni SAA and PtO₂. (b) Pt L₃-edge EXAFS in R space from Pt/Ni SAA with Pt foil and PtO₂ as references. XPS spectra of (c) Pt 4 f and (d) Ni 2 p.

and *H exhibited the highest energy barrier.

We further evaluated the electronic structure of the Pt/Ni (111) surface through DFT to analyze its reactivity [29]. As shown in Fig. S9 the electrons were accumulated in the Pt-Ni bonding region. Doping with Pt caused electrons to move from the surface Ni to the active Pt centers. The Bader charge analysis showed that 0.57 electrons were transferred from bulk Ni to the Pt atoms. For the *CH dehydrogenation step, Fig. S9c and S9d revealed the charge variation occurring during dehydrogenation of *CH to *C and *H. The dehydrogenation process was accompanied by electron transfer from the catalyst surface to the adsorbed molecules. Specifically, the negative charge on hydrogen increased as the reaction progressed. The differential charge density shown in Fig. S9b indicated electron transfer between the Pt/Ni (111) surface and the *CH adsorbate, which implied that Pt donated electrons to the H atom. The negatively charged hydrogen and negatively charged carbon repelled each other, which weakened the C-H bond. Briefly, breaking of the C-H bond required activation of the hydrogen atom, which required electron donation from Pt. Therefore, Pt atoms doping enhanced the CH₄ pyrolysis activity of Ni balls.

To further understand the contribution of mechanical action to CH₄ pyrolysis, the energy released from elastic deformation was used to examine the effects of mechanical vibration. It was worth noting that the images for the Pt/Ni SAA surface temperature from the infrared camera presented a slight heat difference before and after 30 min of vibration, and the temperature increase induced by collisions was not the determining factor that boosted CH₄ pyrolysis in this system (Fig. S10). In addition, the relationship between metal collision and deformation is calculated. Specifically, the influence of longitudinal strain on transverse strain, known as the Poisson effect, was taken into account. Detailed calculation method was presented in SI (Fig. S11). The post-collision model was then subjected to three-dimensional deformation, as shown in Fig. S7b, and it exhibits 10 % compression in the Z direction and 3 % extensions in both the X and Y directions. Since the

dehydrogenation step of *CH to *C and *H shows the highest energy barrier, we simulated this step on the deformed surface. The DFT calculations revealed that the energy barrier on this surface was 26.06 kcal/mol, which was 3.23 kcal/mol lower than that of the invisible variable model. The transition state geometries of CH dissociation on the Pt/Ni (111) surface suggested that H could migrate from C to the top of the Pt atom. This suggested that enhancing the adsorption capability of active metal atoms could facilitate H dissociation from C-H bonds and enhance its migration to active metals, promoting H₂ generation. The partial density of states (PDOS) in Fig. 4 showed that the d-band center (ϵ_d) of Pt before and after deformation are -2.32 eV and -2.19 eV, respectively. The PDOS analysis presented that the ϵ_d of Pt on deformed Ni (111) surface was 0.13 eV higher than the Pt under static conditions. The higher the ϵ_d of the central metal, the stronger its adsorption capacity. And the enhanced adsorption capacity of Pt was conducive to capture H from *CH, thus reducing the dehydrogenation barrier. Consequently, the surface deformation of Pt/Ni induced by physical collision upshifted the ϵ_d of Pt, which enhanced the hydrogen capture capacity of Pt and reduced the energy barrier for the C-H bond scission.

3.4. Catalytic stability of Pt/Ni single-atom alloy and carbon black utilization

Fig. 5a presented the lifetime profiles of CH₄ pyrolysis over Pt/Ni SAA, and the TOF in form of H₂ generation coupled with mechanical vibration was maintained at 1530 h⁻¹ (350 h), achieving state-of-the-art catalytic stability. For the initial 100 h, the conversion of CH₄ decreased slightly, which was related with side reactions and immature active sites during induction stage. First, some inevitable oxygen species in vessel and NiO species could react with CH₄ to produce CO_x as side reactions (CH₄ + 2 [O] = CO₂ + 2 H₂ or CH₄ + [O] = CO + 2 H₂), which improved CH₄ conversion at first but weakened gradually until complete

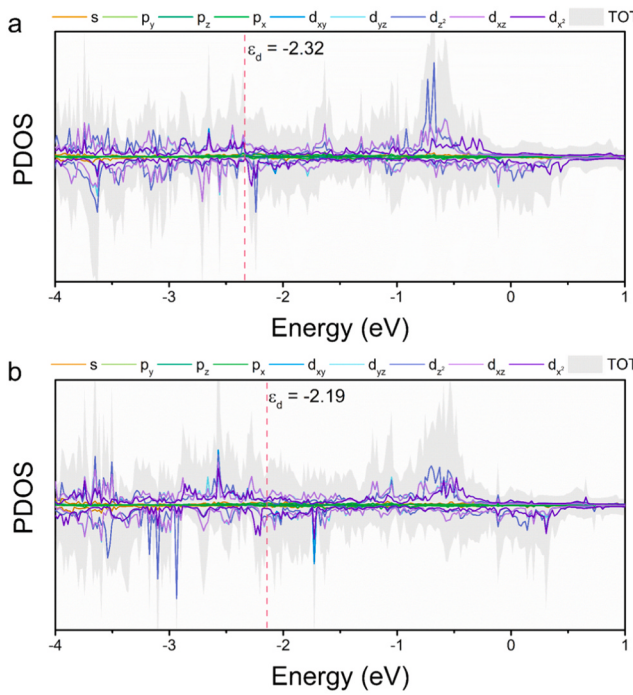


Fig. 4. Partial density of states (PDOS) of different orbitals of Pt on initial Ni (111) surface (a) and deformed Ni (111) surface (b). The Fermi level is set to zero.

consumption of oxygen species. Besides, some active Pt-Ni sites were covered by dissociated carbon species and could not be regenerated timely, which also caused the decline trend of CH₄ conversion until the

equilibrium stage. The XPS spectra showed the existence of O species, which could induce CH₄ oxidation to CO_x, which was proven by the detected CO_x signal during the initial 1000 min (Fig. S12a). Nevertheless, the side reaction was gradually weakened until active oxygen species were completely consumed. Finally, as the only gas product, H₂ had completely come from methane pyrolysis (Fig. S12b). Compared with the pyrolysis performance under static condition in Fig. 1a, mechanical vibration method greatly extended the reaction stability to 350 h without further deactivation. At 215 h in Fig. 5a, the reaction was stopped to remove separable carbon powder in the reactor, and the TOF of H₂ over spent Pt/Ni SAA could recovered after 20 h running at 450 °C and maintained the identical reaction rate again. In addition to CH₄ pyrolysis, we also examined the alkane pyrolysis performance using ethane and propane, and the ethane and propane conversions and H₂ concentrations in effluent were presented in Fig. 5b and c. It was clear that this mechanical catalysis paradigm was also effective for ethane pyrolysis and propane pyrolysis, and the ethane and propane conversion could retain at 52 % and 41 % after at least 50 h running on stream. For propane pyrolysis reaction, the apparent activation energy (Fig. S13) under vibration condition and static condition also illustrated the boosting impact of mechanical vibration on apparent Ea decline and pyrolysis efficiency increase. Since the Pt/Ni SAA exhibited superior catalytic stability during mechanical alkane pyrolysis process, the XANES data for the Pt L₃-edge over spent Pt/Ni sample in Fig. S14 were utilized to identify the stable Pt/Ni alloy structure. Pt atoms in the Pt L₃-edge spectra presented lower white line intensity than Pt foil, proving the reduced state of Pt atoms and the electron donation from Ni to Pt on spent Pt/Ni SAA. EXAFS spectra in k-space (Fig. S14b) and Fourier transform spectra in R-space (Fig. S14c) also revealed that the band length for the first shell on the Pt/Ni SAA was still 2.3 Å, and the different amplitudes between Pt foil and Pt/Ni SAA in k-space proved no Pt particles or PtO₂ appeared on Ni metal surface after long time pyrolysis reaction. Herein, it was concluded the stable Pt/Ni alloy structure

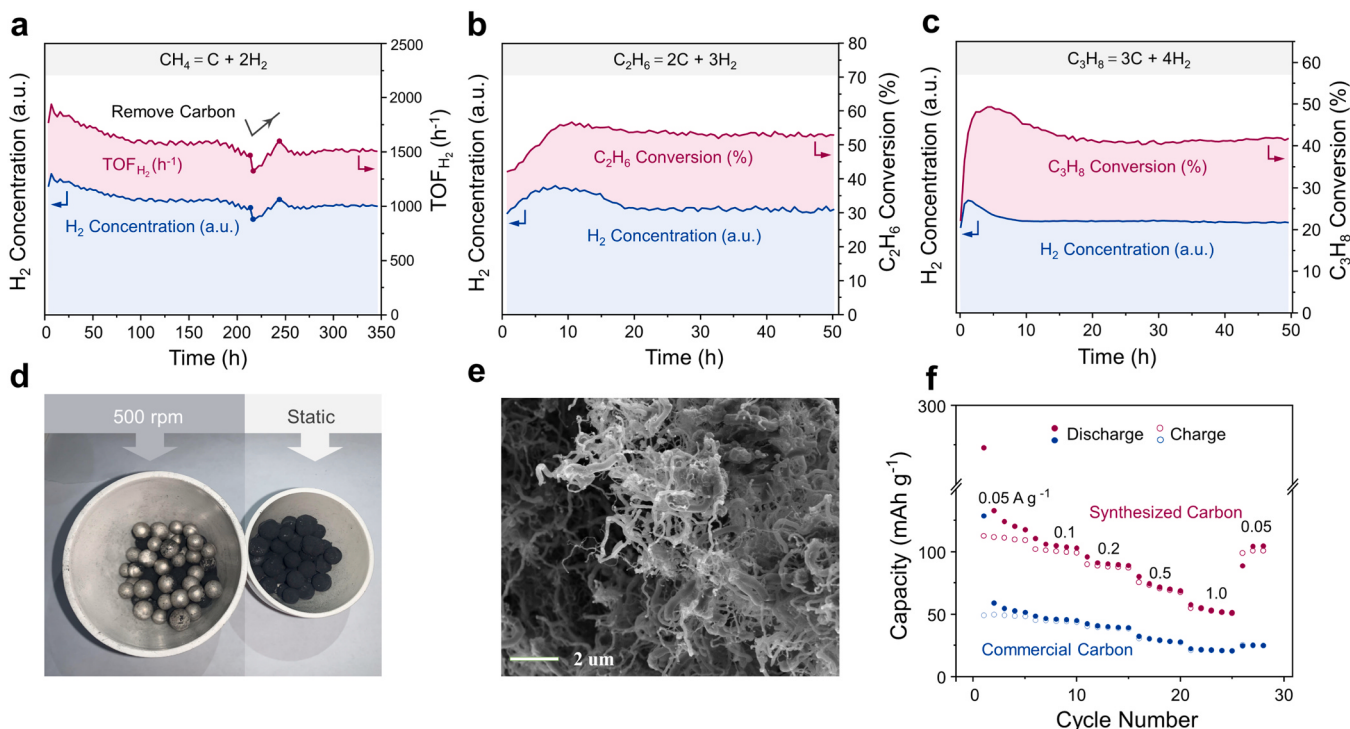


Fig. 5. (a) Lifetime study of CH₄ pyrolysis over Pt/Ni SAA with 500 r/min vibration at 450 °C. The pyrolysis performance of (b) ethane and (c) propane under mechanical condition over Pt/Ni SAA in 50 hrs. Reaction conditions: 100 mL/min 10 % C₂H₆ (C₃H₈) / 90 % N₂, 450 °C, 500 r/min. (d) Used Pt/Ni SAA after the lifetime evaluation. The left side with clean metal surface was spent Pt/Ni SAA under vibration mode, and the right side with carbon surrounded surface was spent Pt/Ni SAA under static mode. (e) SEM images of the obtained carbon products. (f) The rate performance of as-synthesized carbon and commercial electrodes from 0.05 to 1 A·g⁻¹.

ensured the catalytic stability in this work. Besides, compared with the clean metal ball surface after reaction under mechanical vibration (Fig. 5d), the metal balls used under static conditions were surrounded by deposited carbon. This comparison illustrated that deactivation was dominated by carbon deposition during CH₄ pyrolysis, and mechanical vibration removed the deposited carbon in a timely manner. In addition, the EDS spectrum in Fig. S15 for the generated carbon product showed that no Pt signal was detected within the whole record frame, which revealed the good mechanical stability of the Pt/Ni SAA. Finally, the light-off test in Fig. S16 showed that mechanochemical assistance enabled CH₄ pyrolysis above 260 °C, which was interesting and not reported during the thermocatalytic process so far.

To further increase the economic benefit of CH₄ pyrolysis under vibration condition, the carbon product was also collected and reused. First, a BET study (Fig. S17) indicated the mesoporous structure with surface area of 57.6 m²/g, and the SEM images in Fig. 5e and Fig. S18 showed nanorod shapes for the carbon powder. The XRD profile (Fig. S19) and Raman spectrum (Fig. S20) indicated that the collected carbon product was carbon black. To enhance carbon black's application potential, it was used as an electrode material to assess its sodium storage capability. Fig. 5f presents a comparison of the rate performance between the as-synthesized carbon black and commercial graphite electrodes at current densities ranging from 0.05 to 1 A·g⁻¹. The as-synthesized carbon black electrode demonstrates superior reversible capacities of 120, 105, 90, 70, and 52 mA·h·g⁻¹ at 0.05, 0.1, 0.2, 0.5, and 1 A·g⁻¹, respectively. Therefore, it can be asserted that their rate performance was much better compared to that of commercial graphite. In addition, when the current density was returned to 0.05 A·g⁻¹, the as-synthesized carbon black electrode recovered its capacity of 104 mA·h·g⁻¹, which demonstrated its good electrochemical reversibility. Moreover, it exhibited good cycling stability (Fig. S21), maintaining a reversible capacity of 56 mA·h·g⁻¹ after 200 cycles at 1 A·g⁻¹. In comparison to commercial graphite, the product from methane conversion exhibits superior cycling performance. The successful application of obtained carbon black demonstrated the high atom economy of this alkane pyrolysis reaction without carbon emission.

Herein, we also compared the CH₄ pyrolysis performance between previous reports in literature and Pt/Ni SAA in Fig. 6. Pt/Ni SAA as a catalyst for mechanocatalysis method achieved state-of-the-art CH₄ conversion rate, longer lifetime and lower reaction temperature in lab-scale. On the condition that the generated carbon powder could be removed timely and continuously without interval through dedicate design of mechanical reactor, this alkane pyrolysis technology through mechanocatalysis method possesses a great practical application potential.

4. Conclusion

This work designed a Pt/Ni SAA as a robust catalyst and employed mechano-catalysis approach in a homemade ball milling reactor to achieve catalytic alkane pyrolysis. The intact Pt-Ni single atomic alloy structure and timely removal of generated carbon products via mechanical collision enabled 350 h lifetime without deactivation. Compared with thermocatalysis of CH₄ pyrolysis, the introduction of mechanical energy further improved the CH₄ conversion efficiency from 3.1 % to 6.1 % at 450 °C, and triggered CH₄ pyrolysis since 260 °C. The macroscopic collision process with the microscopic theoretical model deformation was linked through the stress generated by the collision, and the subsequent lattice distortion induced the ε_d of Pt upshift, which aided the dehydrogenation of CH*. Since the mechanical energy only occupied ~ 1 % input energy under 450 °C, it was concluded that the mechanical energy efficiency was much higher than thermal energy. Though Pt/Ni SAA was also active for mechanical ethane pyrolysis and propane pyrolysis reaction, additional studies about catalysts structure and reactor design were still necessary to achieve desired H₂ yield and improve application potential of this process. Additionally, more *in situ*

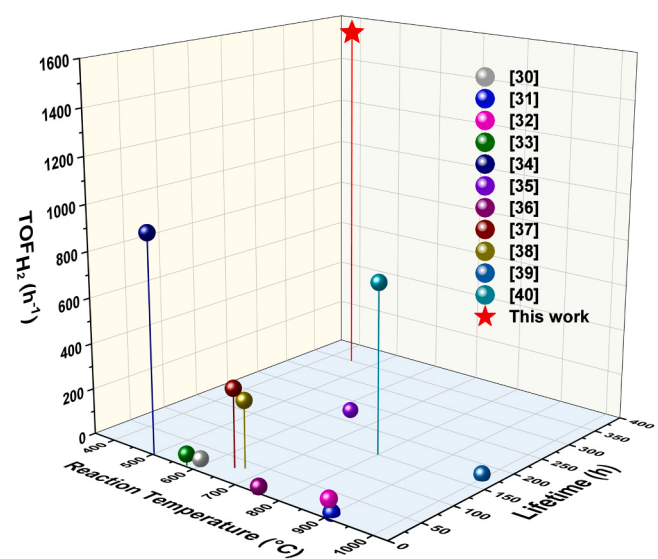


Fig. 6. The catalysts TOF_{H₂}, lifetime and reaction temperature comparison between reports in literatures and this work [30–40].

characterization should be developed to examine the carbon growth on Pt-Ni SAA and reflect the transfer mechanism from mechanical energy to chemical reaction in mechanical reactor. This work provides a possible route for industrial pure H₂ production in absence of carbon emission, meanwhile, it is meaningful to report an alternative option to solve the carbon deposition on catalysts and metallic sites sintering via mechano-catalysis approach.

CRediT authorship contribution statement

Xu Fang: Formal analysis. Ling Zhang: Data curation. Junxia Yang: Data curation. Weiqiao Deng: Writing – review & editing, Supervision, Funding acquisition, Conceptualization. Tie Yu: Writing – review & editing, Supervision, Methodology, Investigation, Funding acquisition, Formal analysis, Data curation. Guoqing Ren: Writing – review & editing. Xiuqin Ci: Data curation. Yuchun Xu: Formal analysis. Hongyan Yang: Writing – original draft, Formal analysis. Rui Tu: Writing – original draft, Investigation, Formal analysis. Jikai Sun: Writing – original draft, Software, Investigation, Formal analysis.

Declaration of Competing Interest

The authors declare that they have no known competing financial interests or personal relationships that could have appeared to influence the work reported in this paper.

Data Availability

Data will be made available on request.

Acknowledgements

This work was supported by the National Key Research and Development Program of China (No. 2022YFA1503100), the National Natural Science Foundation of China (No. 21525315), the Fundamental Research Funds of Shandong University (No. 2019GN111), State Key Laboratory of Catalysis funds of Dalian Institute of Chemical Physics (N-22-16) and the Shandong University Future Program for Young Scholars (No. 62460082064083). The authors are grateful for the technical support for Nano-X from Suzhou Institute of Nano-Tech and Nano-Bionics, Chinese Academy of Sciences (SINANO). The authors thank Xiaoju Li and Haiyan Sui from Shandong University Core Facilities for

Life and Environmental Sciences for their help with the morphology characterization.

Appendix A. Supporting information

Supplementary data associated with this article can be found in the online version at doi:10.1016/j.apcatb.2024.124085.

References

- [1] R.T. O'Neill, R. Boulatov, The many flavours of mechanochemistry and its plausible conceptual underpinnings, *Nat. Rev. Chem.* 5 (3) (2021) 148–167.
- [2] K. Kubota, Y.D. Pang, A. Miura, H. Ito, Redox reactions of small organic molecules using ball milling and piezoelectric materials, *Science* 366 (6472) (2019) 1500–1504.
- [3] S. Ndayiragije, Y.F.; Zhang, Y.Q.; Zhou, Z.; Song, N.; Wang, T.; Majima, L.H.; Zhu, Mechanochemically tailoring oxygen vacancies of MnO₂ for efficient degradation of tetrabromobisphenol A with peroxyomonosulfate, *Appl. Catal. B-Environ.* 307 (2022) 121168.
- [4] S.E. Zhu, F. Li, G.W. Wang, Mechanochemistry of fullerenes and related materials, *Chem. Soc. Rev.* 42 (18) (2013) 7535–7570.
- [5] S.L. James, C.J. Adams, C. Bolm, D. Braga, P. Collier, T. Friscic, F. Grepioni, K.D. M. Harris, G. Hyett, W. Jones, A. Krebs, J. Mack, L. Maini, A.G. Orpen, I.P. Parkin, W.C. Shearouse, J.W. Steed, D.C. Waddell, Mechanochemistry: opportunities for new and cleaner synthesis, *Chem. Soc. Rev.* 41 (1) (2012) 413–447.
- [6] G.F. Han, P. Zhang, P. Scholzen, H.J. Noh, M.Y. Yang, D. Kweon, J.P. Jeon, Y. H. Kim, S.W. Kim, S.P. Han, A.S. Andreev, G. Lang, K. Ihm, F. Li, J.B.D. de Lacarrière, J.B. Baek, Extreme enhancement of carbon hydrogasification via mechanochemistry, *Angew. Chem. Int. Ed.* 61 (2022) 18.
- [7] G.F. Han, F. Li, Z.W. Chen, C. Coppex, S.J. Kim, H.J. Noh, Z.P. Fu, Y.L. Lu, C. V. Singh, S. Siahrostami, Q. Jiang, J.B. Baek, Mechanochemistry for ammonia synthesis under mild conditions, *Nat. Nanotechnol.* 16 (3) (2021) 325–330.
- [8] P. Baláz, M. Achimovičová, M. Baláz, P. Billik, Z. Cherkzova-Zheleva, J.M. Criado, F. Delogu, E. Dutková, E. Gaffet, F.J. Gotor, R. Kumar, I. Mitov, T. Rojac, M. Senna, A. Strelets'kií, K. Wieczorek-Ciurowa, Hallmarks of mechanochemistry: from nanoparticles to technology, *Chem. Soc. Rev.* 42 (18) (2013) 7571–7637.
- [9] B. Szczęśniak, S. Borysiuk, J. Choma, M. Jaroniec, Mechanochemical synthesis of highly porous materials, *Mater. Horiz.* 7 (6) (2020) 1457–1473.
- [10] S. Reichle, M. Felderhoff, F. Schut, Mechano-catalytic room-temperature synthesis of ammonia from its elements down to atmospheric pressure, *Angew. Chem. Int. Ed.* 60 (50) (2021) 26385–26389.
- [11] J.N. Pring, D.M. Fairlie, The methane equilibrium, *J. Chem. Soc. Trans.* 101 (1912) 91–103.
- [12] M. Pudukudy, Z. Yaakob, Q.M. Jia, M.S. Takriff, Catalytic decomposition of methane over rare earth metal (Ce and La) oxides supported iron catalysts, *Appl. Surf. Sci.* 467 (2019) 236–248.
- [13] M. Pudukudy, Z. Yaakob, Methane decomposition over Ni, Co and Fe based monometallic catalysts supported on sol gel derived SiO₂ microflakes, *Chem. Eng. J.* 262 (2015) 1009–1021.
- [14] M. Pudukudy, Z. Yaakob, M.S. Takriff, Methane decomposition into CO_x free hydrogen and multiwalled carbon nanotubes over ceria, zirconia and lanthanum supported nickel catalysts prepared via a facile solid state citrate fusion method, *Energ. Convers. Manag.* 126 (2016) 302–315.
- [15] N. Sanchez-Bastardo, R. Schlögl, H. Ruland, Methane pyrolysis for zero-emission hydrogen production: a potential bridge technology from fossil fuels to a renewable and sustainable hydrogen economy, *Ind. Eng. Chem. Res.* 60 (32) (2021) 11855–11881.
- [16] Y.B. Lu, Z.H. Zhang, H.M. Wang, Y. Wang, Toward efficient single-atom catalysts for renewable fuels and chemicals production from biomass and CO₂, *Appl. Catal. B-Environ.* 292 (2021) 120162.
- [17] Y.Q. Zhang, Single atoms on a roll, *Nat. Rev. Chem.* 2 (4) (2018).
- [18] C.Z. Zhu, S.F. Fu, Q.R. Shi, D. Du, Y.H. Lin, Single-atom electrocatalysts, *Angew. Chem. Int. Ed.* 56 (45) (2017) 13944–13960.
- [19] Z.L. Xu, Z.M. Ao, M. Yang, S.B. Wang, Recent progress in single-atom alloys: synthesis, properties, and applications in environmental catalysis, *J. Hazard. Mater.* 424 (2022).
- [20] G.X. Pei, X.Y. Liu, A.Q. Wang, A.F. Lee, M.A. Isaacs, L. Li, X.L. Pan, X.F. Yang, X. D. Wang, Z.J. Tai, K. Wilson, T. Zhang, Ag alloyed Pd single-atom catalysts for efficient selective hydrogenation of acetylene to ethylene in excess ethylene, *ACS Catal.* 5 (6) (2015) 3717–3725.
- [21] M.D. Marcinkowski, M.T. Darby, J.L. Liu, J.M. Wimble, F.R. Lucci, S. Lee, A. Michaelides, M. Flytzani-Stephanopoulos, M. Stamatakis, E.C.H. Sykes, Pt/Cu single-atom alloys as coke-resistant catalysts for efficient C-H activation, *Nat. Chem.* 10 (3) (2018) 325–332.
- [22] Q. Wang, J.H.; Gong, H.; Zhang, Q.Y. Fan, L. Xue, J.F.; Wu, J.X. Li, Y. Wang, Z.; Liu, R. Gao, S.H. Zeng, Co-promotion of two-type active sites: PtCu_x single-atom alloy and copper-ceria interface for preferential oxidation of CO, *Appl. Catal. B-Environ.* 306 (2022) 121117.
- [23] C.J. Yang, Z.L. Miao, F. Zhang, L. Li, Y.T. Liu, A.Q. Wang, T. Zhang, Hydrogenolysis of methyl glycolate to ethanol over a Pt-Cu/SiO₂ single-atom alloy catalyst: a further step from cellulose to ethanol, *Green. Chem.* 20 (9) (2018) 2142–2150.
- [24] B.T. Qiao, A.Q. Wang, X.F. Yang, L.F. Allard, Z. Jiang, Y.T. Cui, J.Y. Liu, J. Li, T. Zhang, Single-atom catalysis of CO oxidation using Pt-1/FeOx, *Nat. Chem.* 3 (8) (2011) 634–641.
- [25] C.Y. Ling, Y.X. Ouyang, Q. Li, X.W. Bai, X. Mao, A.J. Du, J.L. Wang, A general two-step strategy-based high-throughput screening of single atom catalysts for nitrogen fixation, *Small Methods* 3 (9) (2019).
- [26] J. Gu, G.X. Lan, Y.Y. Jiang, Y.S. Xu, W. Zhu, C.H. Jin, Y.W. Zhang, Shaped Pt-Ni nanocrystals with an ultrathin Pt-enriched shell derived from one-pot hydrothermal synthesis as active electrocatalysts for oxygen reduction, *Nano Res.* 8 (5) (2015) 1480–1496.
- [27] M. García-Dieguez, E. Finocchio, M.A. Larrubia, L.J. Alemany, G. Busca, Characterization of alumina-supported Pt, Ni and PtNi alloy catalysts for the dry reforming of methane, *J. Catal.* 274 (1) (2010) 11–20.
- [28] L.H. Zhu, T. Zheng, C.L. Yu, J.B. Zheng, Z.B. Tang, N.W. Zhang, L. Shu, B.H. Chen, Platinum-nickel alloy nanoparticles supported on carbon for 3-pentanone hydrogenation, *Appl. Surf. Sci.* 409 (2017) 29–34.
- [29] V. Wang, N. Xu, J.C. Liu, G. Tang, W.T. Geng, VASPKIT: a user-friendly interface facilitating high-throughput computing and analysis using VASP code, *Comput. Phys. Commun.* 267 (2021).
- [30] A. Venugopal, S. Naveen Kumar, J. Ashok, D. Hari Prasad, V. Durga Kumari, K.B. S. Prasad, M. Subrahmanyam, Hydrogen production by catalytic decomposition of methane over Ni/SiO₂, *Int. J. Hydrog. Energy* 32 (12) (2007) 1782–1788.
- [31] J.L. Figueiredo, J.J.M. Orfão, A.F. Cunha, Hydrogen production via methane decomposition on Raney-type catalysts, *Int. J. Hydrog. Energy* 35 (18) (2010) 9795–9800.
- [32] D. Torres, S. de Llobet, J.L. Pinilla, M.J. Lázaro, I. Suelves, R. Moliner, Hydrogen production by catalytic decomposition of methane using a Fe-based catalyst in a fluidized bed reactor, *J. Nat. Gas. Chem.* 21 (4) (2012) 367–373.
- [33] B. Zapata, M.A. Valenzuela, J. Palacios, E. Torres-García, Effect of Ca, Ce or K oxide addition on the activity of Ni/SiO₂ catalysts for the methane decomposition reaction, *Int. J. Hydrog. Energy* 35 (21) (2010) 12091–12097.
- [34] K. Tapia-Parada, G. Valverde-Aguilar, A. Mantilla, M.A. Valenzuela, E. Hernández, Synthesis and characterization of Ni/Ce-SiO₂ and Co/Ce-TiO₂ catalysts for methane decomposition, *Fuel* 110 (2013) 70–75.
- [35] G. Wang, Y. Jin, G. Liu, Y. Li, Production of hydrogen and nanocarbon from catalytic decomposition of methane over a Ni-Fe/Al₂O₃ catalyst, *Energy Fuels* 27 (8) (2013) 4448–4456.
- [36] N. Bayat, M. Rezaei, F. Meshkani, Hydrogen and carbon nanofibers synthesis by methane decomposition over Ni-Pd/Al₂O₃ catalyst, *Int. J. Hydrog. Energy* 41 (12) (2016) 5494–5503.
- [37] J. Ashok, P.S. Reddy, G. Raju, M. Subrahmanyam, A. Venugopal, Catalytic decomposition of methane to hydrogen and carbon nanofibers over Ni-Cu-SiO₂ catalysts, *Energy Fuels* 23 (1) (2009) 5–13.
- [38] H. Wang, R.T.K. Baker, Decomposition of methane over a Ni–Cu–MgO catalyst to produce hydrogen and carbon nanofibers, *J. Phy. Chem. B* 108 (52) (2004) 20273–20277.
- [39] D.C. Upham, V. Agarwal, A. Khechfe, Z.R. Snodgrass, M.J. Gordon, H. Metiu, E. W. McFarland, Catalytic molten metals for the direct conversion of methane to hydrogen and separable carbon, *Science* 358 (6365) (2017) 917–921.
- [40] L.N. Chen, Z.G. Song, S.C. Zhang, C.K. Chang, Y.C. Chuang, X.X. Peng, C. Dun, J. J. Urban, J.H. Guo, J.L. Chen, D. Prendergast, M. Salmeron, G.A. Somorjai, J. Su, Ternary NiMo-Bi liquid alloy catalyst for efficient hydrogen production from methane pyrolysis, *Science* 381 (6660) (2023) 857–861.